Cortex Segmentation: A Fast Variational Geometric Approach

Roman Goldenberg*, Ron Kimmel, Ehud Rivlin, and Michael Rudzsky

***Abstract*—An automatic cortical gray matter segmentation from a three-dimensional (3-D) brain images [magnetic resonance (MR) or computed tomography] is a well known problem in medical image processing. In this paper, we first formulate it as a geometric variational problem for propagation of two coupled bounding surfaces. An efficient numerical scheme is then used to implement the geodesic active surface model. Experimental results of cortex segmentation on real 3-D MR data are provided.**

***Index Terms*—Cortical surface segmentation, deformable coupled surfaces, geodesic active contours, level-sets.**

I. Introduction

THE CEREBRAL cortex is the outermost layer of the brain bounded by the outer cortical surface [cerebral spinal fluid (CSF)—gray matter interface] and the inner cortical surface (gray matter—white matter interface). Determining the location of the cortical surface of the human brain is often a first step in brain visualization and analysis. Due to the complicated and convoluted nature of the cortex, the manual slice by slice segmentation is generally a difficult, inefficient and inaccurate process, which makes an automatic three-dimensional (3-D) cortex segmentation an important task.

A significant number of techniques have been proposed to deal with the problem. The whole set of approaches can be roughly divided into two groups: region-based methods and boundary detection methods. Here, we concentrate on one promising direction that is based on deformable surfaces. Deformable surface is a 3-D analog of the active contour model that was introduced in [19], [39] as the "snake model" and is based on minimizing an energy along a curve. Caselles *et al.* [5] and Malladi *et al.* [28] introduced a geometric flow that includes internal and external geometric measures. Later, the geodesic active contour model derived from a reparameterization invariant functional was proposed as a geometric alternative for the snakes [6], [7], [20], [36]. Efficient numerical methods were developed for accelerating of deformable surfaces propagation and some of them were applied for brain segmentation, e.g., see [27]. A combination of fuzzy segmentation and deformable surface model for cortex reconstruction was reported in [42].

The idea to use several interacting deformable contours or surfaces for segmentation was exploited by several research teams. Samson *et al.* [33] proposed a supervised classification model to find an image partition composed of homogeneous regions, assuming the number of classes and their intensity properties are known. The classification problem was formulated using a variational framework aimed to propagate mutually exclusive regular curves toward class region boundaries. Paragios and Deriche [31] presented an image segmentation approach that incorporates boundary and region information sources under a curve-based minimization framework (see, also, [8] for a related effort). The propagating interfaces are coupled by demanding a nonoverlapping set of curves that restricts each pixel to belong to only one region. Bertalmio *et al.* [2] used two implicit surfaces to track regions of interest on surfaces that are being deformed using the level-set methods.

More recently, there has been an effort to apply constraints imposed by the cortex structure properties for better segmentation. Davatzikos *et al.* [14], [13] used the homogeneity of intensity levels within the gray matter region to introduce a force that would drive a deformable surface toward the center of the gray matter layer. Teo *et al.* [38] used the connectivity of the gray matter as a constraint in building the cortex representation by growing out from the white matter boundary. MacDonald *et al.* [24]–[26] proposed to use an intersurface proximity constraint in a two surface model of the inner and outer cortex boundaries in order to guarantee that surfaces do not intersect themselves or each other. Finally, Zeng *et al.* [43] used the fact that the cortical layer has a nearly constant thickness to design a coupled surfaces model in such a way that a special propagation speed term forces the intersurface distance to remain within a predefined range. Later, Gomes and Faugeras implemented the coupled surfaces model for cortex segmentation suggested by Zeng *et al.* [43] using a scheme that preserves the level-set surface representation function as a distance map, so that it is not required to reinitialize it every iteration [16].

In this paper, we adopt the coupled surfaces principle and develop a new model using a variational geometric framework. Unlike the model in [43], the surface propagation equations are not empirically formulated, but derived from a minimization problem. As a result, additional terms are introduced to the surface propagation equations. Our implementation is based on advanced numerical schemes for surface evolution that yield a geometrically consistent and computationally efficient technique.

Manuscript received June 27, 2001; revised September 11, 2002. This work was supported in part by the German-Israeli Foundation (GIF). The Associate Editor responsible for coordinating the review of this paper and recommending its publication was B. Vemuri. *Asterisk indicates corresponding author*.

*R. Goldenberg is with the Computer Science Department, Technion-Israel Institute of Technology, Technion City, Haifa 32000, Israel (e-mail: romang@cs.technion.ac.il).

R. Kimmel, E. Rivlin, and M. Rudzsky are with the Computer Science Department, Technion - Israel Institute of Technology, Technion City, Haifa 32000, Israel.

Digital Object Identifier 10.1109/TMI.2002.806594

II. The Geometric-Variational Approach

A. Coupled Surfaces Segmentation as a Minimization Problem

Let $\mathcal{S}(u, v)$: $\mathbb{R}^2 \rightarrow \mathbb{R}^3 = (x(u, v), y(u, v), z(u, v))$ be a parameterized two-dimensional (2-D) surface in 3-D space. Using the active contour approach, a boundary segmentation can be seen as a weighted area minimization problem

$$\min_{\mathcal{S}} \int g(x, y, z)\, da = \min_{\mathcal{S}} \int g(\mathcal{S}(u, v))|\mathcal{S}_u \times \mathcal{S}_v|\, du\, dv$$

where da is an area element and $g(x, y, z)$: $\mathbb{R}^3 \rightarrow \mathbb{R}^+$ is a positive boundary indicator function that depends on the image. It gets small, close to zero values along the boundary and higher values elsewhere.

In order to extract the cortical layer, we have to find its two bounding surfaces: The outer CSF—gray matter interface, and the inner gray matter— white matter interface.

Theoretically, if one could provide perfect boundary indicator functions both for the inner and outer interfaces—$g_{\text{in}}()$ and $g_{\text{out}}()$—it would have been sufficient to use a single surface approach, i.e., to find the inner and outer bounding surfaces $\mathcal{S}^{\text{in}}$ and $\mathcal{S}^{\text{out}}$ by separate minimization of the two uncoupled functionals

$$\mathcal{S}^{\text{in}} = \arg\min_{\mathcal{S}} \int g_{\text{in}}\, da, \quad \mathcal{S}^{\text{out}} = \arg\min_{\mathcal{S}} \int g_{\text{out}}\, da. \quad (1)$$

In practice, the limitations imposed by the imaging devices often result in noisy and inaccurate image data, which reduce the reliability of boundary detectors that use only local information, e.g., voxel intensity, gradient, etc.

That is the main reason for incorporating additional constraints imposed by the nature of the problem. In the case of cortex segmentation it was suggested to use the fact that the cortical layer has a nearly constant thickness (about 3 mm) [3]. Zeng *et al.* [43] designed a coupled surfaces model where two deformable surfaces are kept within a predefined normal range from each other by specially designing the interface propagation speed in such a way that it decreases whenever surfaces are getting too far or too close.

Let us adopt a similar coupled surfaces approach, but, rather than heuristically building an expression for the surface propagation speed [43], we shall derive it from a minimization problem. This time, unlike in (1), we want a simultaneous minimization of both interfaces $\mathcal{S}^{\text{in}}$ and $\mathcal{S}^{\text{out}}$, so that the minimum is reached when $\mathcal{S}^{\text{in}}$ captures the CSF—gray matter boundary and $\mathcal{S}^{\text{out}}$ locks on to the white matter—gray matter boundary. We start with

$$\left(\mathcal{S}^{\text{in}}, \mathcal{S}^{\text{out}}\right) = \arg \min_{\mathcal{S}^{\text{in}}, \mathcal{S}^{\text{out}}} \left[\int_{\mathcal{S}^{\text{in}}} g_{\text{in}}\, da + \int_{\mathcal{S}^{\text{out}}} g_{\text{out}}\, da\right]. \quad (2)$$

Motivated by [43], we link between the two surfaces, and introduce an additional component that penalizes the deviations of the intersurface distance from the normal range, which yields the functional

$$\begin{aligned}
&\mathcal{F}\left(\mathcal{S}^{\text{in}}, \mathcal{S}^{\text{out}}\right) \\
&\quad = \int_{\mathcal{S}^{\text{in}}} h\left[d\left((x, y, z), \mathcal{S}^{\text{out}}\right)\right] g_{\text{in}}(x, y, z)\, da \\
&\qquad + \int_{\mathcal{S}^{\text{out}}} h\left[d\left((x, y, z), \mathcal{S}^{\text{in}}\right)\right] g_{\text{out}}(x, y, z)\, da \\
&\quad = \int_{\mathcal{S}^{\text{in}}} h\left[d\left(\mathcal{S}^{\text{in}}(u, v), \mathcal{S}^{\text{out}}\right)\right] g_{\text{in}}\left(\mathcal{S}^{\text{in}}(u, v)\right) \\
&\qquad \cdot \left|\mathcal{S}_u^{\text{in}} \times \mathcal{S}_v^{\text{in}}\right| du\, dv + \int_{\mathcal{S}^{\text{out}}} h\left[d\left(\mathcal{S}^{\text{out}}(u, v), \mathcal{S}^{\text{in}}\right)\right] \\
&\qquad \cdot g_{\text{out}}\left(\mathcal{S}^{\text{out}}(u, v)\right) \cdot \left|\mathcal{S}_u^{\text{out}} \times \mathcal{S}_v^{\text{out}}\right| du\, dv \qquad (3)
\end{aligned}$$

where $d((x, y, z), \mathcal{S})$ is the Euclidean distance of the point (x, y, z) from the surface $\mathcal{S}$, i.e., $d(\overline{x}, \mathcal{S}) = \min_{\overline{x}_s \in \mathcal{S}}\{\|\overline{x} - \overline{x}_s\|\}$, and $h(\text{dist})$ is a penalty function that gets a constant low value when the distances are within the "normal" range and grows fast otherwise, see Fig. 1.

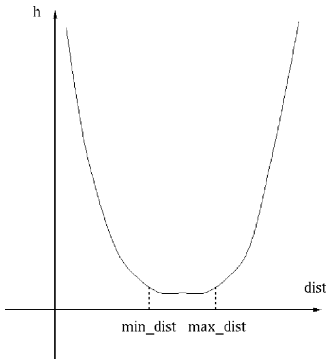

Fig. 1. The "h" function gets low constant value in the normal range.

It is clear that the minimum of the functional (3) is reached when both surfaces are located at their corresponding cortex boundaries and the intersurface distance is preferably kept within the normal range.

B. Level-Set Formulation

The Osher–Sethian [30] level-set method is a numerical technique for analyzing evolving interface motion that works on a fixed coordinate system and considers an evolving front in an implicit form

$$\mathcal{S} = \{(x, y, z)|\Phi(x, y, z) = 0\}.$$

The basic idea is to evolve the 3-D embedding function Φ: $\mathbb{R}^3 \rightarrow \mathbb{R}$ so that its zero level set would always track the current position of the evolving surface $\mathcal{S}$. Let us denote the set of 2-D surfaces defined by different level sets of Φ by $\mathcal{S}(u, v, \phi)$. Then, the original surface is defined as $\mathcal{S}(u, v) = \mathcal{S}(u, v, \phi)|_{\phi=0}$.

One can prove (see Appendix A) that close to the interface ($\phi = 0$), for any function $f(x, y, z)$

$$\int_{\phi}\int_{u}\int_{v} f\left|\mathcal{S}_u^{\text{in}} \times \mathcal{S}_v^{\text{in}}\right| du\, dv\, d\phi = \int_{x}\int_{y}\int_{z} f|\nabla\phi|\, dx\, dy\, dz.$$

Then, the functional $\mathcal{F}(\mathcal{S}^{\text{in}}, \mathcal{S}^{\text{out}})$ can be expressed as

$$\begin{aligned}
&\int_{\phi}\int_{u}\int_{v} h\left[d\left(\mathcal{S}^{\text{in}}(u, v, \phi), \mathcal{S}^{\text{out}}\right)\right] g_{\text{in}}\left(\mathcal{S}^{\text{in}}(u, v, \phi)\right) \\
&\quad \cdot \left|\mathcal{S}_u^{\text{in}} \times \mathcal{S}_v^{\text{in}}\right| du\, dv\, d\phi + \int_{\phi}\int_{u}\int_{v} \\
&\quad \cdot h\left[d\left(\mathcal{S}^{\text{out}}(u, v, \phi), \mathcal{S}^{\text{in}}\right)\right] \cdot g_{\text{out}}(\mathcal{S}^{\text{out}}(u, v, \phi)) \\
&\quad \cdot \left|\mathcal{S}_u^{\text{out}} \times \mathcal{S}_v^{\text{out}}\right| du\, dv\, d\phi \\
&= \int_{x}\int_{y}\int_{z} h\left[d\left((x, y, z), \mathcal{S}^{\text{out}}\right)\right] g_{\text{in}}(x, y, z) \\
&\quad \left|\nabla\Phi^{\text{in}}\right| dx\, dy\, dz + \int_{x}\int_{y}\int_{z} h\left[d\left((x, y, z), \mathcal{S}^{\text{in}}\right)\right] \\
&\quad \cdot g_{\text{out}}(x, y, z)\left|\nabla\Phi^{\text{out}}\right| dx\, dy\, dz. \qquad (4)
\end{aligned}$$

Essentially, (4) enables us to implement surface evolution on the fixed x, y, z coordinate system. Besides its important property of automatic handling topological changes of the evolving surface, the level-set approach gives us a very simple and stable way to compute the distance used as an argument of the h function. Since the implicit representation of the evolving surface does not imply any restrictions on the form of the embedding function, we are free to define the Φ function as a distance map. Then, the distance from a point (x, y, z) to the surface $\mathcal{S}$, defined by the zero level set of the embedding function Φ, is simply $\Phi(x, y, z)$. Therefore, the expression in (4) can be rewritten as

$$\begin{aligned}
&\mathcal{L}\left(\Phi^{\text{in}}, \Phi^{\text{out}}\right) \\
&= \int_{x}\int_{y}\int_{z} h\left(\Phi^{\text{out}}(x, y, z)\right) g_{\text{in}}(x, y, z)\left|\nabla\Phi^{\text{in}}\right| dx\, dy\, dz \\
&\quad + \int_{x}\int_{y}\int_{z} h\left(\Phi^{\text{in}}(x, y, z)\right) g_{\text{out}}(x, y, z) \\
&\quad \cdot \left|\nabla\Phi^{\text{out}}\right| dx\, dy\, dz \qquad (5)
\end{aligned}$$

subject to Φ^{in} and Φ^{out} are distance extensions from their zero sets, and we are looking for

$$\left(\Phi^{\text{in}}, \Phi^{\text{out}}\right) = \arg\min_{\Phi^{\text{in}}, \Phi^{\text{out}}} \mathcal{L}\left(\Phi^{\text{in}}, \Phi^{\text{out}}\right).$$

Taking the variation with respect to Φ^{in} and Φ^{out} and writing it as a gradient descent flow yields the system

$$\begin{aligned}
\frac{d\Phi^{\text{in}}}{dt} &= \operatorname{div}\left[h\left(\Phi^{\text{out}}\right) g_{\text{in}}(x, y, z)\frac{\nabla\Phi^{\text{in}}}{\left|\nabla\Phi^{\text{in}}\right|}\right] \\
&\quad + \frac{dh(\Phi^{\text{in}})}{d\Phi^{\text{in}}} g_{\text{out}}(x, y, z)\left|\nabla\Phi^{\text{out}}\right| \\
\frac{d\Phi^{\text{out}}}{dt} &= \operatorname{div}\left[h\left(\Phi^{\text{in}}\right) g_{\text{out}}(x, y, z)\frac{\nabla\Phi^{\text{out}}}{\left|\nabla\Phi^{\text{out}}\right|}\right] \\
&\quad + \frac{dh(\Phi^{\text{out}})}{d\Phi^{\text{out}}} g_{\text{in}}(x, y, z)\left|\nabla\Phi^{\text{in}}\right|. \qquad (6)
\end{aligned}$$

There exists one limitation to the model developed so far. As the system uses only local information, it can be trapped by a meaningless local minimum, unless initialized close to the desired boundary. In order to overcome this difficulty we apply an additional force that comes from volume maximization and motivated by the balloon force [12]. We add the following weighted volume maximization terms to the functional:

$$\alpha\left[\iiint_{V^{\text{in}}} g_{\text{in}}(x, y, z)\, dV + \iiint_{V^{\text{out}}} g_{\text{out}}(x, y, z)\, dV\right], \qquad (7)$$

where dV is a volume element, V^{in} and V^{out} are the interiors of the regions enclosed by the surfaces S^{in} and S^{out}, respectively, and α is a negative constant. It is equivalent to applying a pressure force outward. The volume element is modulated by the edge indicator function g in order to stop the surface expansion near the desired boundary. The Euler–Lagrange for the terms in (7) is of the form $\alpha g\vec{n}$, where $\vec{n}$ is a normal to the surface (see proof in Appendix B and [44] for similar development in 2-D), and in level-set formulation this yields

$$\begin{aligned}
\frac{d\Phi^{\text{in}}}{dt} &= \operatorname{div}\left[h\left(\Phi^{\text{out}}\right) g_{\text{in}}\frac{\nabla\Phi^{\text{in}}}{\left|\nabla\Phi^{\text{in}}\right|}\right] \\
&\quad + \frac{dh(\Phi^{\text{in}})}{d\Phi^{\text{in}}} g_{\text{out}}\left|\nabla\Phi^{\text{out}}\right| + \alpha g_{\text{in}}\left|\nabla\Phi^{\text{in}}\right| \\
\frac{d\Phi^{\text{out}}}{dt} &= \operatorname{div}\left[h\left(\Phi^{\text{in}}\right) g_{\text{out}}\frac{\nabla\Phi^{\text{out}}}{\left|\nabla\Phi^{\text{out}}\right|}\right] \\
&\quad + \frac{dh(\Phi^{\text{out}})}{d\Phi^{\text{out}}} g_{\text{in}}\left|\nabla\Phi^{\text{in}}\right| + \alpha g_{\text{out}}\left|\nabla\Phi^{\text{out}}\right|. \qquad (8)
\end{aligned}$$

C. Numerical Scheme

An explicit Euler scheme with forward time derivative introduces a numerical limitation on the time step needed for stability. Moreover, the whole domain needs to be updated each step, which is a time consuming operation. In order to cope with these limitations, we use the fast geodesic active contours approach [15] which is based on the Weickert–Romeny–Viergever [41] semi-implicit additive operator splitting (AOS) scheme and uses the narrow-band approach to limit the computation to a tight region of few grid points around the zero level set [9], [1].

We rely on the fact that the embedding function Φ is a distance map. Gomes and Faugeras [16] proposed an approach, where the Hamilton–Jacobi equation used to evolve the distance function is replaced by a partial differential equation that preserves the Φ function as a distance map (see also [37]), which was applied for cortex segmentation using the coupled surfaces model suggested in [43]. Here, we reinitialize the Φ function every iteration using the fast marching method [35], [34], [40], which is a computationally optimal numerical method for distance computation on rectangular grids. The method has a computational complexity bound of $O(N)$, where N is the number of points in the narrowband as shown by Tsitsiklis [40], and requires a set of grid points with a known exact distance to the zero level set for initialization. Those seed points are detected with subpixel accuracy using an algorithm motivated by the "marching cubes" algorithm [23], [10]. For every grid cube within the narrowband where the Φ function changes its sign we find the distance to the zero level set for each one of the eight cube vertices. The cube is split into five pyramids [Fig. 2(a)] and within each

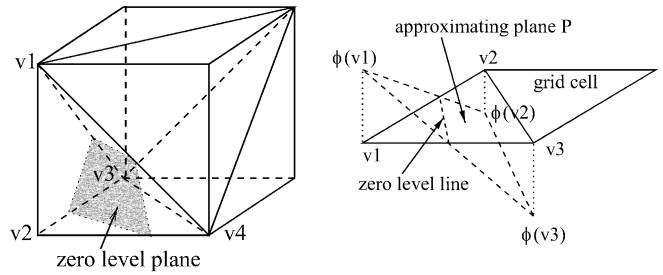

(a) (b)

Fig. 2. (a) Grid cube split into five pyramids. (b) Finding distance to the zero level curve (2-D case).

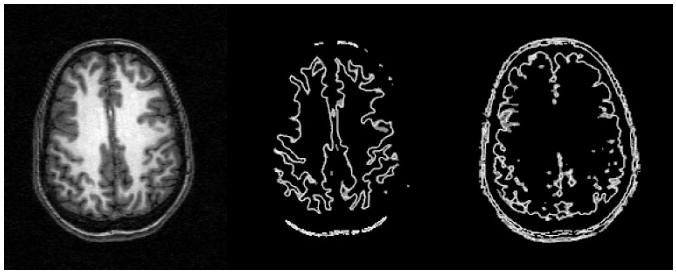

(a) (b) (c)

Fig. 3. Boundary indicator functions. (a) A slice from the original MR image. (b) Result of the inner boundary detection operator. (c) Result of the outer boundary detection operator.

pyramid the Φ function is approximated by a four-dimensional (4-D) hyperplane.

In order to clarify this idea let us first explore the low-dimensional case where a 2-D curve is implicitly given by the zero level of a function Φ: $\mathbb{R}^2 \rightarrow \mathbb{R}$ [Fig. 2(b)]. A grid cell is split into two triangles and there exists one and only one plane, P, going through the points $\Phi(v_1)$, $\Phi(v_2)$, and $\Phi(v_3)$, where v_1, v_2, and v_3 are the triangle vertices. The values of the Φ function at the vertices are then updated to the distance between the vertex and the zero level line of P. Each vertex adopts the minimal of all its updates.

Going back to the 3-D case, let $\overline{n}_{4\times 1}$ be a vector defining a hyperplane in 4-D going through the four points $\Phi(v_1)$, $\Phi(v_2)$, $\Phi(v_3)$, and $\Phi(v_4)$ [Fig. 2(a)], so that the hyperplane equation is given by $\overline{n}^T\overline{x} = \Phi$, where $\overline{x}$ is a 3-D point written in homogeneous coordinates. The plane $\overline{n}$ can be found by solving the system of four linear equations $\{\overline{n}^T\overline{v_i} = \Phi(v_i),\ i = 1, \ldots, 4\}$. Then, the zero level set of hyperplane $\overline{n}$ is a plane in 3-D given by $\overline{n}^T\overline{x} = 0$. The distances we are looking for are the distances from vertices v_i to the zero level plane. One should verify that the normal vector from the v_i to the zero level plane is inside the pyramid. Otherwise, the shortest distance on the intersection of the plane with the pyramid boundary is taken instead.

The procedure above is repeated each iteration for both inner and outer surfaces and the corresponding narrowbands automatically modify their shapes as we reinitialize the distance maps. As one can see from (6), when updating Φ^{in} the values of Φ^{out} are needed to be defined within the area of Φ^{in} numerical support, and *vice a versa*. Therefore, it is important to ensure that the narrowband of one surface includes the other. This can be done using asymmetric narrowbands as in [43], or using a single narrowband for both surfaces.

III. Experimental Results

In order to apply our method to cortex segmentation we have yet to determine appropriate boundary indicator functions for the inner and outer interfaces: g_{in} and g_{out}. Significant number of techniques have been proposed to deal with the problem, e.g., adaptive fuzzy segmentation in [32], Bayesian approach in [17], etc. Here, we adopt a simplified version of an operator used by Zeng *et al.* [43], measuring the likelihood of a voxel to be on the boundary between two tissues. It is assumed that statistical distributions P_{CSF}, P_g and P_w of the image intensities are known for each one of the three tissues—CSF, gray matter, and white matter respectively. The probability of a voxel V to be on the boundary between tissue A and tissue B is estimated from the difference between the probability measures integrated over a neighborhood of V. Namely, for the gray matter/white matter and the CSF/gray matter interfaces these probabilities are given by

$$P_{g/w}(V) = \left(1 + \lambda \left| \sum_{V_i \in N(V)} (P_g(V_i) - P_w(V_i)) \right| \right)^{-1} \tag{9}$$

and

$$P_{\text{CSF}/g}(V) = \left(1 + \lambda \left| \sum_{V_i \in N(V)} (P_{\text{CSF}}(V_i) - P_g(V_i)) \right| \right)^{-1} \tag{10}$$

and the inner and outer boundary indicator functions are then defined as

$$g_{\text{in}}(V) = \frac{1}{1 + \mu(P_{g/w}(V))^2} \tag{11}$$

and

$$g_{\text{out}}(V) = \frac{1}{1 + \mu(P_{\text{CSF}/g}(V))^2} \tag{12}$$

respectively, where $N(V)$ is a neighborhood of the voxel V and λ and μ are parameters. Fig. 3 shows the result of applying the inner and outer boundary detectors on a single slice from the original MR brain image.

It should be noted that the model for tissue intensity priors we used here is an oversimplified one. In practice, in order to provide a fully automatic segmentation solution, one should be able to cope with the problem of intensity nonuniformity in MR images due to the imaging equipment limitations, nonlinear gain artifacts, and patient-induced electrodynamic interactions. Although the issue is beyond the scope of this paper, we only mention that very promising results have been achieved using Bayesian methods (for example [21], [22], and recently [29]) combined with brain atlas-based registration and with active contour segmentation as in [18]. In this sense, the algorithm presented here can be used as a building block in conjunction with the methods reported elsewhere.

We still need to set initial conditions (the initial position of the surfaces) in order to start the segmentation process. This

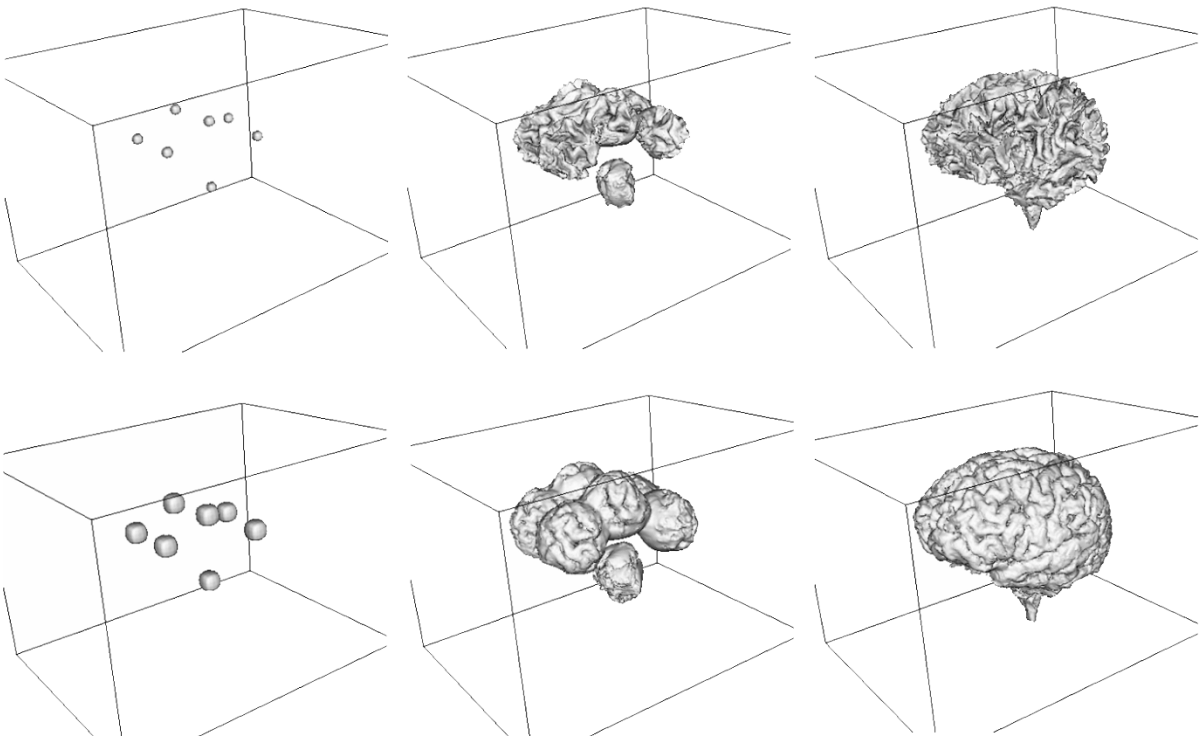

(a) (b) (c)

Fig. 4. Coupled surfaces propagation. (top) Inner surface and (bottom) outer surface. (a) Initial position. (b) Intermediate state. (c) Final result.

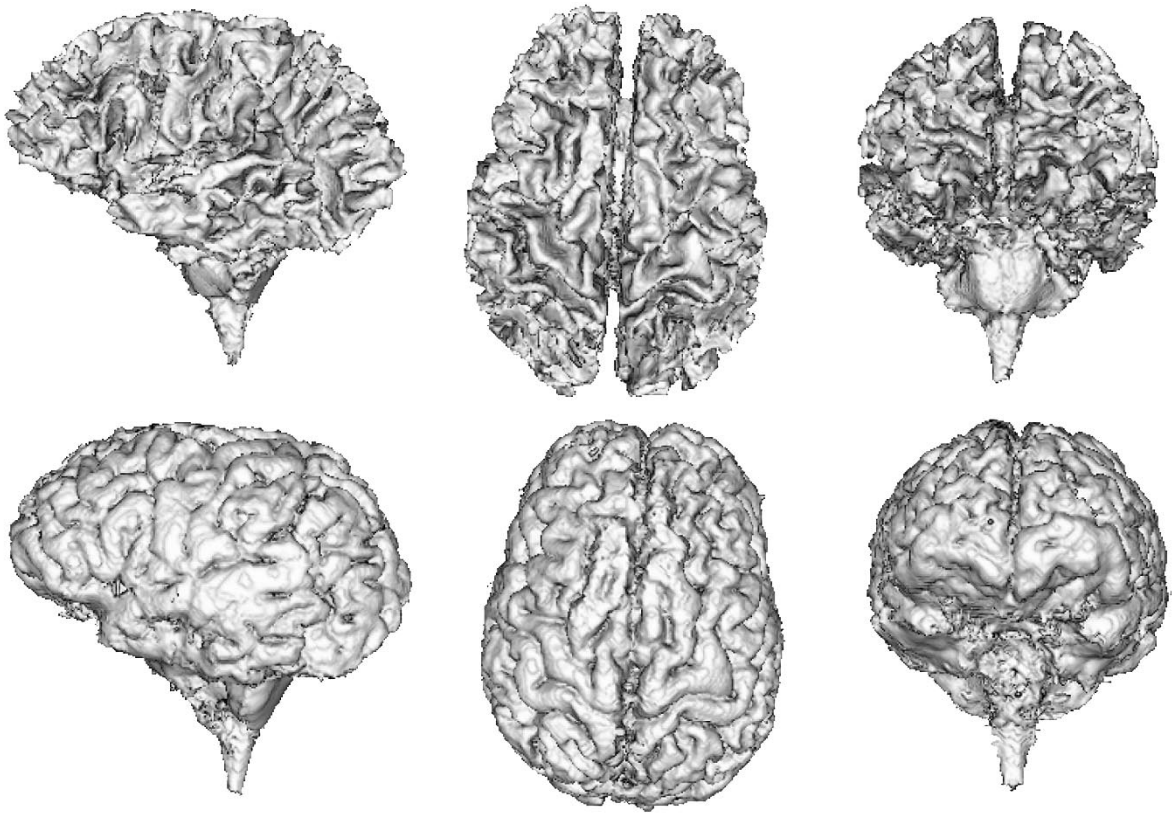

(a) (b) (c)

Fig. 5. Different views of the reconstructed cortical surfaces. (top) Inner surface. (bottom) Outer surface. (a) Sagittal view. (b) Axial view. (c) Coronal view.

is done by manually choosing several seed points inside the white matter region and building two small concentric surfaces (e.g., spheres or cubes) at the normal distance from each other. Fig. 4(a) shows an initial condition with seven "seeds."

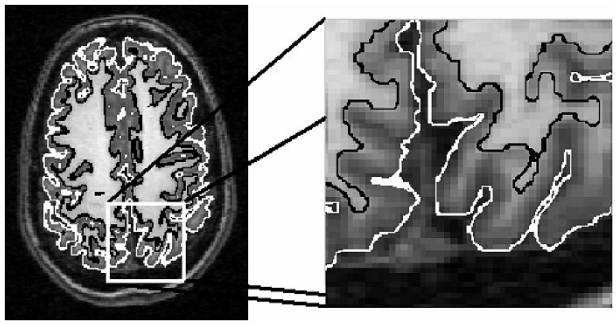

Fig. 6. Extracted boundaries in a single-slice section and a zoom into a small region. White contour: outer surface; black contour: inner surface.

The coupled surfaces then propagate outwards, driven by a balloon force multiplied by the boundary indicator function, while maintaining the intersurface distance, which is controlled by the h function (3). Finally, the interfaces converge to their exact boundary position that minimize the weighted area and maximal volume as determined by the functionals (4) and (7). The process terminates when the surfaces do not change for two time steps. Fig. 4(b) and (c) shows an intermediate state and the final result. Both inner and outer surfaces are shown.

The three standard views (sagittal, axial, and coronal) of the segmented outer and inner cortical surfaces are presented in Fig. 5 and a zoom-in of the extracted boundaries for a single slice is shown in Fig. 6.

For a 192 $\times$ 250 $\times$ 170 MR image of the whole brain, our algorithm runs in about 2.5 min on a Pentium III PC.

We performed a validation test on the BrainWeb [11] data available at [4]. The data set was generated from the normal brain database using the $T1$ modality, 1-mm slice thickness, 3% noise level and 20% intensity nonuniformity settings. Fig. 7 presents the comparison results for six different slices. The top row shows the ground truth data from the BrainWeb database and the middle row presents the segmentation results obtained using our algorithm. The bottom row is an overlap of the two above, where the dark gray color shows the correctly detected cortex regions. Regions not found by the algorithm are shown in white, and black designates areas mistakenly marked by the algorithm as cortex. The segmentation results are nearly identical to the ground truth data, except a systematic one-pixel-wide error on the boundary (white on the outer surface and black on the inner surface). The error can be caused by a number of reasons including a mismatch in the priors used in building the ground truth data and by our algorithm in estimating the CSF/gray matter/white matter image intensities, and the technique used to extract the boundary from the zero level set—taking positive instead of negative voxels may shift the region boundary by one pixel.

IV. Concluding Remarks

In this paper, we presented a new approach for cortex segmentation. The method is based on the coupled surfaces model that was derived as a minimization problem in a variational geometric framework. The surface evolution is performed using the fast geodesic active contour approach—an efficient numerical scheme combining semi-implicit AOS propagation scheme, level-set representation, narrow-band approach and the fast marching method. An efficient technique is proposed for the zero level-set reconstruction in 3-D. Cortex segmentation results from a real MR brain images and BrainWeb synthetic data demonstrate the computational efficiency and accuracy of the new method.

Appendix A

Let $S(u, v) = \{x(u, v), y(u, v), z(u, v)\}$ be a parameterized surface and let $S = \{(x, y, z)|\phi(x, y, z) = 0\}$ be its implicit representation. That is, we can consider a family of surfaces $S(u, v, \phi)$ where $S(u, v) = S(u, v, \phi)|_{\phi=0}$. Then, close to the zero level set

$$\int_\phi\int_u\int_v f\left|\mathcal{S}_u^{\text{in}} \times \mathcal{S}_v^{\text{in}}\right| du\, dv\, d\phi = \int_x\int_y\int_z f|\nabla\phi|\, dx\, dy\, dz$$

where $f(x, y, z)$ is a function defined over the integration domain.

Proof: Recall that $\int\int\int du\, dv\, d\phi = \int\int\int |J|^{-1}\, dx\, dy\, dz$, where the Jacobian is given by $J = \langle (x_u, y_u, z_u) \times (x_v, y_v, z_v), (x_\phi, y_\phi, z_\phi)\rangle$. In our case, for the general parameterized surface $S(u, v)$ and its implicit representation $\phi(x, y, z) = 0$, the normal to the surface is given by

$$\vec{N} = \frac{S_u \times S_v}{|S_u \times S_v|} = \frac{\nabla\phi}{|\nabla\phi|}.$$

Therefore

$$S_u \times S_v = |S_u \times S_v|\vec{N} = |S_u \times S_v|\,\frac{\nabla\phi}{|\nabla\phi|}.$$

We also know that $1 = d\phi/d\phi = \langle\nabla\phi, (x_\phi, y_\phi, z_\phi)\rangle$. Thus, $S_\phi = (x_\phi, y_\phi, z_\phi) = \nabla\phi/|\nabla\phi|^2$ and the Jacobian is given by

$$\begin{aligned} J &= \langle S_u \times S_v, S_\phi\rangle = \left\langle S_u \times S_v, \frac{\nabla\phi}{|\nabla\phi|^2}\right\rangle \\ &= \left\langle |S_u \times S_v|\,\frac{\nabla\phi}{|\nabla\phi|}, \frac{\nabla\phi}{|\nabla\phi|^2}\right\rangle = \frac{|S_u \times S_v|}{|\nabla\phi|}. \end{aligned}$$

We can now conclude with

$$\begin{aligned} &\int_\phi\int_u\int_v f(S(u, v, \phi))\left|\mathcal{S}_u^{\text{in}} \times \mathcal{S}_v^{\text{in}}\right| du\, dv\, d\phi \\ &\quad= \int_x\int_y\int_z f(x, y, z)|J|^{-1}\left|\mathcal{S}_u^{\text{in}} \times \mathcal{S}_v^{\text{in}}\right| dx\, dy\, dz \\ &\quad= \int_x\int_y\int_z f(x, y, z)|\nabla\phi|\, dx\, dy\, dz. \end{aligned}$$

■

Appendix B

Let us derive the Euler–Lagrange equation for the functional

$$E[S(u, v)] = \int\int\int_V f(x, y, z)\, dx\, dy\, dz \qquad (13)$$

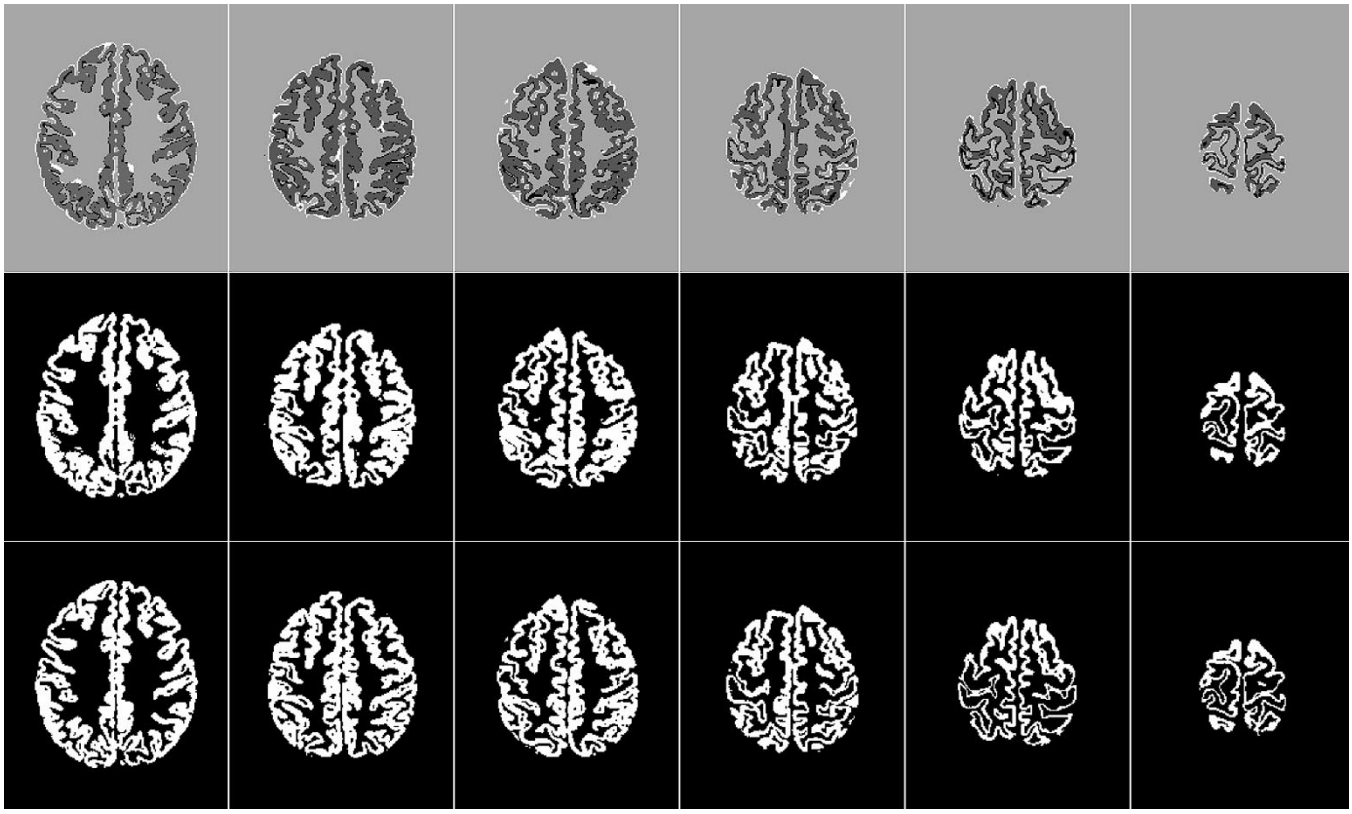

Fig. 7. Comparison with the "BrainWeb" data set. (top) Ground truth. (middle) Gray matter regions extracted by our algorithm (bottom) Overlap image. Gray color designates regions both the ground truth and the algorithm agree upon. Regions not found by the algorithm are shown in white and regions mistakenly found by the algorithm are shown in black.

where the $S(u, v) = \{x(u, v), y(u, v), z(u, v)\}$ is a 2-D boundary surface of a 3-D volume V parameterized by two parameters u and v.

Let $\mathcal{G}(x, y, z) = (P(x, y, z), Q(x, y, z), R(x, y, z))$ be a vector field defined on V in the following way:

$$P(x, y, z) = \tfrac{1}{3}\int_0^x f(t, y, z)\,dt$$
$$Q(x, y, z) = \tfrac{1}{3}\int_0^y f(x, t, z)\,dt$$
$$R(x, y, z) = \tfrac{1}{3}\int_0^z f(x, y, t)\,dt.$$

Then, $\mathrm{div}\mathcal{G} = f(x, y, z)$ and, assuming P, Q, and R are in $\mathcal{C}^1$ on V, by Gauss theorem

$$E[S] = \iiint_V \mathrm{div}\mathcal{G}\,dV = \iint_S P\,dy\,dz + Q\,dz\,dx + R\,dx\,dy.$$

Changing the integration variables to u and v, yields

$$\begin{aligned} E[S] &= \iint_S (P[y_u z_v - z_u y_v] + Q[z_u x_v - x_u z_v] \\ &\qquad + R[x_u y_v - y_u x_v])\,du\,dv \\ &= \iint_S \mathcal{G}\cdot(S_u \times S_v)\,du\,dv = \iint_S \mathcal{G}\cdot\vec{n}_{(u,v)}\,da \end{aligned}$$

where $\vec{n}_{(u,v)}$ is the unit normal to the surface S and $da = |S_u \times S_v|\,du\,dv$ is a geometric area element.

Let us denote

$$L(x, y, z, x_u, x_v, y_u, y_v, z_u, z_v) = \mathcal{G}\cdot(S_u \times S_v).$$

Then, the Euler–Lagrange equations for $E[S]$ are

$$\frac{\delta E}{\delta x} = \frac{\partial L}{\partial x} - \frac{\partial}{\partial u}\frac{\partial L}{\partial x_u} - \frac{\partial}{\partial v}\frac{\partial L}{\partial x_v} \tag{14}$$
$$\frac{\delta E}{\delta y} = \frac{\partial L}{\partial y} - \frac{\partial}{\partial u}\frac{\partial L}{\partial y_u} - \frac{\partial}{\partial v}\frac{\partial L}{\partial y_v} \tag{15}$$
$$\frac{\delta E}{\delta z} = \frac{\partial L}{\partial z} - \frac{\partial}{\partial u}\frac{\partial L}{\partial z_u} - \frac{\partial}{\partial v}\frac{\partial L}{\partial z_v}. \tag{16}$$

Explicitly, (14) is given by

$$\begin{aligned} \frac{\delta E}{\delta x} &= \left(\frac{\partial P}{\partial x}, \frac{\partial Q}{\partial x}, \frac{\partial R}{\partial x}\right)\cdot(S_u \times S_v) \\ &\quad + \frac{\partial Q}{\partial u} z_v - \frac{\partial R}{\partial u} y_v - \frac{\partial Q}{\partial v} z_u + \frac{\partial R}{\partial v} y_u \\ &= \left(\frac{\partial P}{\partial x} + \frac{\partial Q}{\partial y} + \frac{\partial R}{\partial z}\right)(y_u z_v - z_u y_v) \\ &= f(x, y, z)\vec{n}_x \end{aligned}$$

where $\vec{n}_x$ is the x component of the normal vector. Similarly, for (15) and (16) we have

$$\frac{\delta E}{\delta y} = f(x, y, z)\vec{n}_y \quad \text{and} \quad \frac{\delta E}{\delta z} = f(x, y, z)\vec{n}_z.$$

Thus

$$\frac{\delta E}{\delta S} = f(x, y, z)\vec{n}.$$

ACKNOWLEDGMENT

The authors would like to thank Prof. G. Lohmann of Max Planck Institute of Cognitive Neuroscience who kindly provided them with the brain MR images.

REFERENCES

[1] D. Adalsteinsson and J. A. Sethian, "A fast level set method for propagating interfaces," *J. Comp. Phys.*, vol. 118, pp. 269–277, 1995.
[2] M. Bertalmio, G. Sapiro, and G. Randall, "Region tracking on level-sets methods," *IEEE Trans. Med. Imag.*, vol. 18, pp. 448–451, Oct. 1999.
[3] S. M. Blinkov and I. I. Glezer, *The Human Brain in Figures and Tables, A Quantative Handbook*. New York: Plenum, 1968.
[4] Brainweb: Simulated Brain Database. [Online]. Available: http://www.bic.mni.mcgill.ca/brainweb/.
[5] V. Caselles, F. Catte, T. Coll, and F. Dibos, "A geometric model for active contours," *Numerische Mathematik*, vol. 66, pp. 1–31, 1993.
[6] V. Caselles, R. Kimmel, and G. Sapiro, "Geodesic active contours," in *Proc. ICCV'95*, Boston, MA, June 1995, pp. 694–699.
[7] ——, "Geodesic active contours," *IJCV*, vol. 22, no. 1, pp. 61–79, 1997.
[8] T. F. Chan and L. A. Vese, "Active contours without edges," *IEEE Trans. Image Processing*, vol. 10, pp. 266–277, Feb. 2001.
[9] D. L. Chopp, "Computing minimal surfaces via level set curvature flow," *J. Comp. Phys.*, vol. 106, no. 1, pp. 77–91, May 1993.
[10] H. E. Cline, W. E. Lorensen, R. Kikinis, and F. Jolesz, "Three-dimensional segmentation of MR images of the head using probability and connectivity," *J. Comput.-Assist. Tomogr.*, vol. 14, no. 6, pp. 1037–1045, 1990.
[11] C. A. Cocosco, V. Kollokian, R. K.-S. Kwan, and A. C. Evans, "Brainweb: Online interface to a 3-D MRI simulated brain database," *NeuroImage*, vol. 5, no. 4, p. S425, 1997.
[12] L. D. Cohen, "On active contour models and balloons," *CVGIP: Image Understanding*, vol. 53, no. 2, pp. 211–218, 1991.
[13] C. A. Davatzikos and R. N. Bryan, "Using a deformable surface model to obtain a shape representation of the cortex," *IEEE Trans. Med. Imag.*, vol. 15, pp. 785–795, Dec. 1996.
[14] C. A. Davatzikos and J. Prince, "An active contour model for mapping the cortex," *IEEE Trans. Med. Imag.*, vol. 14, pp. 65–80, Mar. 1995.
[15] R. Goldenberg, R. Kimmel, E. Rivlin, and M. Rudzsky, "Fast geodesic active contours," *IEEE Trans. Image Processing*, vol. 10, pp. 1467–1475, Oct. 2001.
[16] J. Gomes and O. Faugeras, "Reconciling distance functions and level sets," in *Lecture Notes in Computer Science*, M. Nielsen, P. Johansen, O. F. Olsen, and J. Weickert, Eds. Berlin, Germany, 1999, vol. 1682, Scale-Space Theories in Computer Vision, pp. 70–81.
[17] M. Joshi, J. Cui, K. Doolittle, S. Joshi, D. Van Essen, L. Wang, and M. I. Miller, "Brain segmentation and the generation of cortical surfaces," *NeuroImage*, vol. 9, no. 5, pp. 461–476, 1999.
[18] T. Kapur, W. E. L. Grimson, W. M. Wells, III, and R. Kikinis, "Segmentation of brain tissue from magnetic resonance images," *Med. Image Anal.*, vol. 1, no. 2, pp. 109–127, 1996.
[19] M. Kass, A. Witkin, and D. Terzopoulos, "Snakes: Active contour models," *Int. J. Comput. Vis.*, vol. 1, pp. 321–331, 1988.
[20] S. Kichenassamy, A. Kumar, P. Olver, A. Tannenbaum, and A. Yezzi, "Gradient flows and geometric active contour models," presented at the ICCV'95, Boston, MA, June 1995.
[21] K. Van Leemput, F. Maes, D. Vandermeulen, and P. Suetens, "Automated model-based bias field correction of mr images of the brain," *IEEE Trans. Med. Imag.*, vol. 18, pp. 885–896, Oct. 1999.
[22] ——, "Automated model-based tissue classification of mr images of the brain," *IEEE Trans. Med. Imag.*, vol. 18, pp. 897–908, Oct. 1999.
[23] W. E. Lorensen and H. E. Cline, "Marching cubes: A high resolution 3-D surface construction algorithm," *ACM Comput. Graphics*, vol. 21, no. 24, pp. 163–169, July 1987.
[24] D. MacDonald, D. Avis, and A. C. Evans, "Multiple surface identification and matching in magnetic resonance images," *Proc. SPIE*, vol. 2359, pp. 160–169, 1994.
[25] ——, "Proximity constraints in deformable models for cortical surface," in *Proc. 1st Int. Conf. Medical Image Computing Computer-Assisted Intervention*, Boston, MA, 1998, pp. 650–659.
[26] D. MacDonald, N. Kabani, D. Avis, and A. C. Evans, "Automated 3-D extraction of inner and outer surfaces of cerebral cortex from MRI," *NeuroImage*, vol. 12, no. 3, pp. 340–356, Sept. 2000.
[27] R. Malladi and J. A. Sethian, "An $O(N \log N)$ algorithm for shape modeling," *Proc. Nat. Academy of Sciences, USA*, vol. 93, pp. 9389–9392, 1996.
[28] R. Malladi, J. A. Sethian, and B. C. Vemuri, "Shape modeling with front propagation: A level set approach," *IEEE Trans. Pattern Anal. Machine Intell.*, vol. 17, pp. 158–175, Feb. 1995.
[29] J. L. Marroquin, B. C. Vemuri, S. Botello, and F. Calderon, "An accurate and efficient Bayesian method for automatic segmentation of brain MRI," in *Proc. ECCV02*, p. IV: 560 ff.
[30] S. J. Osher and J. A. Sethian, "Fronts propagating with curvature dependent speed: Algorithms based on Hamilton–Jacobi formulations," *J. Comp. Phys.*, vol. 79, pp. 12–49, 1988.
[31] N. Paragios and R. Deriche, "Coupled geodesic active regions for image segmentation," presented at the *Eur. Conf. Computer Vision*, Ireland, 2000.
[32] D. L. Pham and J. L. Prince, "Adaptive fuzzy segmentation of magnetic resonance images," *IEEE Trans. Med. Imag.*, vol. 18, pp. 737–752, Sept. 1999.
[33] C. Samson, L. Blanc-Feraud, G. Aubert, and G. J Zerubia, "A level set model for image classification," *Proc. Int. Conf. Scale-Space Theories in Computer Vision*, pp. 306–317, 1999.
[34] J. A. Sethian, *Level Set Methods: Evolving Interfaces in Geometry, Fluid Mechanics, Computer Vision and Materials Sciences*. Cambridge, MA: Cambridge Univ. Press, 1996.
[35] ——, "A marching level set method for monotonically advancing fronts," *Proc. Nat. Acad. Sci.*, vol. 93, no. 4, 1996.
[36] J. Shah, "A common framework for curve evolution, segmentation and anisotropic diffusion," in *Proc. IEEE CVPR'96*, pp. 136–142.
[37] A. Steiner, R. Kimmel, and A. M. Bruckstein, "Shape enhancement and exaggeration," *Graphical Models Image Processing*, vol. 60, no. 2, pp. 112–124, 1998.
[38] P. C. Teo, G. Sapiro, and B. Wandell, "Creating connected representations of cortical gray matter for functional MRI visualization," *IEEE Trans. Med. Imag.*, vol. 16, pp. 852–863, Dec. 1997.
[39] D. Terzopoulos, A. Witkin, and M. Kass, "Constraints on deformable models: Recovering 3-D shape and nonrigid motions," *Artif. Intell.*, vol. 36, pp. 91–123, 1988.
[40] J. N. Tsitsiklis, "Efficient algorithms for globally optimal trajectories," *IEEE Trans. Automat. Contr.*, vol. 40, pp. 1528–1538, Sept. 1995.
[41] J. Weickert, B. M. ter Haar Romeny, and M. A. Viergever, "Efficient and reliable scheme for nonlinear diffusion filtering," *IEEE Trans. Image Processing*, vol. 7, pp. 398–410, Mar. 1998.
[42] C. Xu, D. L. Pham, M. E. Rettmann, D. N. Yu, and J. L. Prince, "Reconstruction of the human cerebral cortex from magnetic resonance images," *IEEE Trans. Med. Imag.*, vol. 18, pp. 467–480, June 1999.
[43] X. Zeng, L. H. Staib, R. T. Schultz, and J. S. Duncan, "Segmentation and measurement of the cortex from 3-D MR images using coupled surfaces propagation," *IEEE Trans. Med. Imag.*, vol. 18, pp. 927–937, Oct. 1999.
[44] S. C. Zhu and A. Yuille, "Region competition: Unifying snakes, region growing, and bayes/MDL for multiband image segmentation," *IEEE Trans. Pattern Anal. Machine Intell.*, vol. 18, pp. 884–900, Sept. 1996.